Physics of the Earth and Planetary Interiors 267 (2017) 9–18

Contents lists available at ScienceDirect

Physics of the Earth and Planetary Interiors

journal homepage: www.elsevier.com/locate/pepi

Effects of water on P-V-T equation of state of pyrope HPSTAR 380-2017

Dawei Fan [a,b], Chang Lu [c], Jingui Xu [b,d], Bingmin Yan [a], Bin Yang [a], Jiuhua Chen [a,e,*]

[a] Center for High Pressure Science and Technology Advanced Research, Changchun 130012, China
[b] Key Laboratory for High Temperature and High Pressure Study of the Earth's Interior, Institute of Geochemistry, Chinese Academy of Sciences, Guiyang 550081, China
[c] Department of Geological Sciences, Jackson School of Geosciences, The University of Texas at Austin, Austin, TX 78712, USA
[d] University of Chinese Academy of Sciences, Beijing 100049, China
[e] Center for the Study of Matter at Extreme Conditions, Department of Mechanical and Materials Engineering, Florida International University, Miami 33199, USA

ARTICLE INFO

Article history:
Received 23 November 2016
Received in revised form 15 February 2017
Accepted 22 March 2017
Available online 24 March 2017

Keywords:
Hydrous pyrope
Equation of state
High temperature and pressure
X-ray diffraction
Diamond anvil cell

ABSTRACT

High-pressure single-crystal/powder synchrotron X-ray diffraction was carried out on a hydrous pure magnesium pyrope ($Mg_3Al_2Si_3O_{12}$) containing 900 ppmw H_2O, synthesized at 4.0 GPa and 1300 K. The pressure-volume (*P-V*) single-crystal data from room pressure to 9.81 GPa at ambient temperature were fitted by a third-order Birch-Murnaghan equation of state (BM-EoS) yielding a unit-cell volume of $V_0 = 1505.14 \pm 0.38$ Å^3, an isothermal bulk modulus of $K_0 = 160 \pm 3$ GPa and its pressure derivative $K'_0 = 5.2 \pm 0.4$. When fixing $K'_0 = 4.0$, the data yielded $V_0 = 1504.58 \pm 0.32$ Å^3 and $K_0 = 166 \pm 2$ GPa. The pressure-volume-temperature (*P-V-T*) EoS of the synthetic hydrous pyrope was also measured at temperatures up to 900 K and pressures up to 16.75 GPa, using a diamond anvil cell in conjunction with *in situ* synchrotron angle-dispersive powder X-ray diffraction. The *P-V* data at room temperature and in a pressure range of 0.0001–14.81 GPa were then analyzed by a third-order BM-EoS and yielded $V_0 = 1505.35 \pm 0.25$ Å^3, $K_0 = 161 \pm 2$ GPa, $K'_0 = 5.0 \pm 0.3$. With K'_0 fixed to 4.0, we also obtained $V_0 = 1505.04 \pm 0.29$ Å^3 and $K_0 = 167 \pm 1$ GPa. Consequently, we fitted the *P-V-T* data with the high-temperature third-order BM-EoS approach and obtained the thermoelastic parameters of $V_0 = 1505.4 \pm 0.3$ Å^3, $K_0 = 162 \pm 1$ GPa, $K'_0 = 4.9 \pm 0.2$, the temperature derivative of the bulk modulus $(\partial K_0/\partial T)_P = -0.018 \pm 0.004$ GPa K^{-1}, and the thermal expansion coefficient at ambient conditions $\alpha_0 = (3.2 \pm 0.1) \times 10^{-5}$ K^{-1}. These properties were consistent with the thermal pressure EoS analysis. These new results on hydrous pyrope were also compared with previous studies of anhydrous pyrope. The main effect of hydration on pyrope is to decrease K_0 and increase K'_0 by increasing the vacancies or unoccupied volume in the structure. The entire dataset enabled us to examine the thermoelastic properties of important mantle garnets and this data has further applications for modeling the P-T conditions in the upper mantle of the Earth's interior using deep mineral assemblages.

1. Introduction

Silicate garnets are nesosilicates with the general formula $X_3Y_2(SiO_4)_3$, where the eight-coordinated dodecahedral X sites are usually occupied by divalent cations (typically Mg, Fe, Mn, or Ca) and the six-coordinated octahedral Y sites by trivalent cations (typically Al, Fe, or Cr). These octahedral/tetrahedral sites form a three-dimensional corner-sharing network which defines interstitial dodecahedral divalent metal sites with eightfold coordination (Smyth et al., 2000). Garnets are widespread minerals in the upper mantle and transition zone of Earth, comprising of up to 40% of the pyrolite composition volume and up to 70% of the eclogitic composition (Akaogi and Akimoto, 1977; Anderson and Bass, 1984; Irifune and Ringwood, 1987; Ita and Stixrude, 1992; Dymshits et al., 2014). Garnets are also important components of the subducted oceanic crust (Irifune and Ringwood, 1993; Kubo et al., 2002) as stable phases in a wide range of pressures and temperatures, and play a fundamental role in many high-pressure and high-temperature petrologic processes (Saltzer et al., 2001; Keshav et al., 2007). As the principal mineral end member of the garnet group, pyrope ($Mg_3Al_2Si_3O_{12}$) is widely accepted as playing an important role in understanding the properties of the upper mantle and transition zone (Sinogeikin and Bass, 2002a,b; Frost, 2008; Fumagalli and Klemme, 2015). Garnet lherzolite models of the upper mantle can contain a pyrope volume about 15% (Boyd et al., 2004; Hunter and Smith, 1981). Pyrope forms a complete solid solution with $MgSiO_3$-majorite (Gasparik, 2000), another garnet found in the upper mantle and transition zone of the Earth. Natural garnets from eclogite xenoliths are usually pyrope-rich (Lu and Keppler, 1997). Therefore, accurate knowledge of the thermoelastic properties of

* Corresponding author at: Center for High Pressure Science and Technology Advanced Research, Changchun 130012, China.
E-mail address: chenjh@hpstar.ac.cn (J. Chen).

http://dx.doi.org/10.1016/j.pepi.2017.03.005
0031-9201/

pyrope is directly relevant for deducing appropriate compositional models, seismic tomographic images, and the velocity and density profiles of the Earth's interior (e.g. Duffy and Anderson, 1989; Weidner and Wang, 2000).

The nominally anhydrous mineral phases in the Earth's upper mantle and transition zone (410–660 km depth) may serve as a large internal reservoir of water which has profound implications for Earth's evolution as a water planet (Ohtani, 2005; Beran and Libowitzky, 2006; Tenner et al., 2009). Water plays important roles in the phase transformation kinetics in the Earth's interior, which affects the mantle dynamics (e.g., Kubo et al., 1998). Trace amounts of dissolved hydrogen defects in nominally anhydrous mantle phases influence the physical properties of mantle materials, such as rheology (e.g., Chen et al., 1998; Mei and Kohlstedt, 2000; Jung and Karato, 2001; Kavner, 2003; Karato, 2006), elasticity (e.g., Jacobsen, 2006), and electrical conductivity (e.g., Karato, 1990; Huang et al., 2005). Much effort has been made estimating the water storage capacity of nominally anhydrous mineral phases to determine factors controlling water incorporation into the structure (e.g., Rossman and Aines, 1991; Kohlstedt et al., 1996; Rossman, 1996; Lu and Keppler, 1997; Withers et al., 1998; Smyth et al., 2003, 2007; Skogby, 2006; Mookherjee and Karato, 2010; Tenner et al., 2012). In the context of water storage at high pressures, garnet is a particularly important phase because grossular ($Ca_3Al_2Si_3O_{12}$) is known to be capable of dissolving up to 20.80 wt% H_2O (Passaglia and Rinaldi, 1984; O'Neill et al., 1993) and significant water content has been found in pyropic garnet from xenoliths (Bell and Rossman, 1992). Water content in garnet also can be used to place constraints on water fugacities (Aines and Rossman, 1984). Trace element zoning in garnet may be used to investigate the P-T paths in metamorphic rocks (Hickmott et al., 1987; Hickmott, 1989). Hydrogen zonation in garnet may be an important source of information about the metamorphic processes that occur during crystal growth (Hickmott, 1989). Since garnet increases in abundance from about 5% volume at a 150 km depth to around 30% at a 650 km depth (Ringwood, 1991), it is important to know whether this phase can dissolve large amounts of water throughout its compositional and P-T stability range. Previous studies have revealed that hydroxyl occurrence in nominally anhydrous mantle phases is closely related to cation vacancy defects (e.g., Ingrin and Skogby, 2000; Skogby, 2006). Moreover, water may be incorporated in garnets as OH^- defects associated with charge balancing or oxidation-reduction reactions, or it may substitute Si in the hydrogarnet substitution (Lu and Keppler, 1997; Withers et al., 1998; Mookherjee and Karato, 2010). Therefore, the hydrous component in garnet has important geological implications for the Earth's mantle, and it is critical to understand the state of water and its role in the structure of garnets in the Earth's interior.

To date, the elasticity of pyrope has been extensively studied using both multi-anvil apparatus and the diamond anvil cell (e.g., Hazen and Finger, 1978; Sato et al., 1978; Levien et al., 1979; Leitner et al., 1980; Leger et al., 1990; Conrad et al., 1999; Zhang et al., 1998; Chen et al., 1999; Wang and Ji, 2001; Sinogeikin and Bass, 2000, 2002a,b; Li et al., 2011). Up to now, most of the pyrope studies have been limited to either high pressure and room temperature or ambient pressure and high temperature, however, there have been few studies that focus on the thermoelastic properties of pyrope (Bonczar and Graham, 1977; Wang et al., 1998; Sinogeikin and Bass, 2002a,b; Gwanmesia et al., 2006; Zou et al., 2012; Lu et al., 2013; Du et al., 2015). Furthermore, to our knowledge, there are no reports about the thermoelasticity of hydrous pyrope at simultaneously high pressure and high temperature, which hinders the accurate determination of appropriate compositional models and density profiles of the Earth's upper mantle.

Here, we investigated the pressure-volume-temperature (*P-V-T*) relations of a synthetic hydrous pyrope at high pressure and high temperature up to 17 GPa and 900 K, using a diamond anvil cell combined with *in situ* synchrotron radiation angle-dispersive X-ray diffraction. The thermoelastic properties of the hydrous pyrope were obtained by fitting the present *P-V-T* data to the high-temperature Birch-Murnaghan (HTBM) EoS and thermal pressure EoS. We also discuss our results with respect to previous reports of the thermoelastic properties of anhydrous pyrope, and evaluate the high pressure-temperature and hydrogen effects on pyrope to aid the current understanding of Earth's deep upper-mantle mineralogical models.

2. Sample and experimental methods

2.1. Sample

The synthesis of hydrous pyrope was carried out using a multi-anvil pressure apparatus (YJ-3000T), at the Institute of Geochemistry, Chinese Academy of Sciences, Guiyang, China. Details of this experimental set-up are described elsewhere by Xie et al. (1993). The pressurization system of this press consisted of six WC anvils, with their tips truncated to 23.5 × 23.5 mm^2, which were simultaneously pushed by six hydraulic rams to generate high pressure in the experimental assembly (Fan et al., 2013). The pressure in the sample chamber was calibrated using a quartz-coesite phase transition and the high-pressure melting curve of copper, with a pressure measurement error margin of less than 1.5%. The temperature in the sample chamber was measured using a Pt-$Pt_{90}Rh_{10}$ thermocouple, with an uncertainty value less than 5 K (Xie et al., 1993, 2002). The starting materials used in the synthesizing experiments were stoichiometric amounts of high purity magnesium oxide (MgO), aluminum oxide (Al_2O_3) and silica (SiO_2). The mixture was then melted at 1 atm and 1700 K, which produced a homogeneous glass after quenching. The homogeneous glass was crushed and ground into a fine powder in acetone and then encapsulated in platinum capsules with 10 wt% of deionised water. The synthesis was carried out at 4.0 GPa and 1300 K with a run duration of 48 h, and perfectly clear and inclusion-free single crystals of pyrope were picked from the charge. The ambient X-ray diffraction data were collected using a D/Max-2200 X-ray diffractometer with graphite crystal monochromator and Cu Kα radiation. The ambient powder X-ray spectrum of pyrope was indexed according to the standard spectra (JCPDS 87-1093), confirming that the structure of the synthetic pyrope was cubic, and belonged to the *Ia3d* space group. The electron probe microanalysis further confirmed that the synthetic sample was a single phase with the composition as follows (in wt%): MgO, 29.9(3); Al_2O_3, 24.9(2); SiO_2, 44.7(2), which can be also written in term of formula unit as $Mg_{3.01}Al_{2.00}Si_{3.01}O_{12}$.

Several crystals were mounted individually in epoxy resin so that doubly-polished crystal slabs could be prepared. After polishing, the crystal slabs were extracted from the resin and cleaned using CCl_4. An electronic micrometer with a 1 μm precision was used to measure the sample thickness, which ranged between 300 and 500 μm. A Nicolet 5700 FTIR spectrometer coupled with a microscope was used to analyze the OH contents of X-ray-oriented, faceted single crystals using a KBr beam-splitter and a liquid-nitrogen cooled MCT-A detector. Measurements were performed through optically clean, inclusion-free, and crack-free areas under a continuous dry air flush. Where samples were large enough, we employed a focused 100 μm spot size on the crystal surface through redundant aperturing. Smaller apertures were used to analyze areas down to 40 × 40 μm. Our synthesized pyropes have an asymmetric peak in the absorption spectrum centered at 3630 cm^{-1} (Fig. 1), which corresponds exactly to those in the OH spectra of synthetic pyropes of previous studies (Geiger et al., 1991; Withers et al., 1998; Mookherjee and Karato, 2010). The water contents were computed from integrated absorbances using the calibration of Bell et al. (1995) for pyrope, which showed that the water content of this hydrous pyrope sample was about 900 ppmw.

2.2. Room-temperature and high-pressure single-crystal X-ray diffraction experiment

Before loading into the diamond anvil cell, the pyrope crystal was examined in air. The refined unit-cell parameters constrained to cubic symmetry are reported in Table 1. The *in situ* room temperature and high-pressure synchrotron single-crystal X-ray diffraction experiments were carried out at the BL15U1 beamline using angle-dispersive diffraction with diamond-anvil cells at the Shanghai Synchrotron Radiation Facility (SSRF). A symmetric-type diamond anvil cell equipped with 500 μm diamond culets was used for pressure generation. A gasket made of stainless steel foil (type T301) with pre-indented thickness of ~ 55 μm and a center hole of 200 μm in diameter served as the sample chamber. The 4:1 methanol-ethanol mixture was used as a pressure-transmitting medium, which is hydrostatic up to 10 GPa as

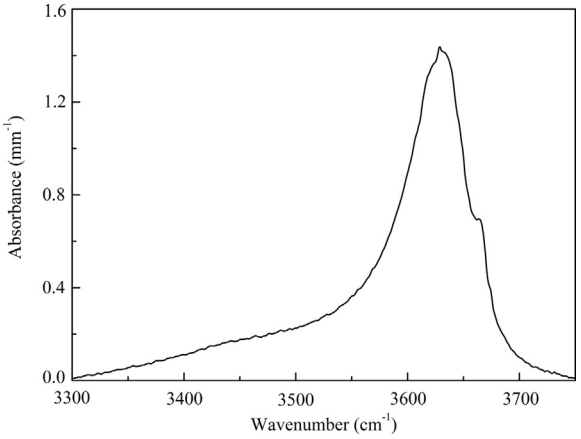

Fig. 1. FTIR spectra of synthetic pyrope garnet for the wave-number range of 3300-3750 cm^{-1}.

Table 1
Unit cell parameters of hydrous pyrope from single-crystal X-ray diffraction data at high pressure and room temperature.

P (GPa)	V (Å^3)
0.0001	1505.24(8)
0.45(3)	1500.52(7)
1.32(11)	1492.75(8)
2.28(37)	1484.54(8)
3.44(28)	1474.38(9)
4.73(36)	1463.56(8)
5.62(47)	1457.87(10)
6.47(38)	1451.35(8)
7.59(43)	1442.13(10)
8.73(52)	1433.85(9)
9.81(48)	1427.22(10)

Numbers in parenthesis represent standard deviations.

demonstrated by Piermarini et al. (1973) and Angel et al. (2007). A ruby chip was loaded as a pressure calibrant together with the hydrous pyrope sample (about 50 × 50 × 25 μm) in the sample chamber. Ruby fluorescence spectra were collected before and after each collection of X-ray diffraction data, and the positions of the R1 and R2 peaks were determined by fitting them with Lorentzian functions. The pressure was calculated from the fitted R1 and R2 peak positions using the method of Mao et al. (1978). Diffraction images were collected using MAR-165 charge coupled device (CCD) detector, placed at a distance of approximately 180 mm to the sample. The detector geometry parameters were calibrated using a CeO_2 diffraction standard. The X-ray beam was monochromatized to a wavelength of 0.6199 Å and focused down to 2 × 3 μm^2 area. Diffraction data were collected while the diamond anvil cell rotated around the vertical axis of the instrument (ω-axis) from −12 to +12°, with a typical exposure time of 0.5 s/°. Diffraction images were analyzed using the GSE_ADA/RSV software package (Dera et al., 2013). Then, the unit-cell parameters of hydrous pyrope were calculated by a least squares technique using Unitcell software (Holland and Redfern, 1997). Each diffraction pattern has at least 30 good single crystal diffraction spots. Except the single crystal diffraction spots of diamond, all the other single crystal diffraction spots could be successfully indexed using the cubic symmetry of pyrope. In the calculation, at least 11 sample diffraction spots were used to refine the unit-cell parameters: (400), (420), (332), (422), (431), (521), (611), (620), (444), (640), and (642).

2.3. High-temperature and high-pressure powder X-ray diffraction experiment

High-temperature and high-pressure experiments were carried out by using a modified Merrill-Bassett type diamond-anvil cell. The culet-size of the diamonds, sample chamber of the gaskets and the pressure-transmitting medium were the same as those in the single crystal diffraction experiment. The hydrous pyrope powders were slightly pressed between two opposing diamond anvils to form an approximately 25 μm thick disk, and a piece of the sample about 100 μm in diameter was loaded into the sample chamber. The cell pressure was determined using the equation of state of gold (pressure marker) as proposed by Fei et al. (2007). Heating was conducted using a resistance-heating system, and the temperature was measured using a $Pt_{90}Rh_{10}$-Pt_{100} thermocouple attached to the pavilion of the diamond anvil. We first compressed the sample up to 10 GPa and then increased the temperature up to 900 K. Heating was maintained at 900 K for about 15 min in order to minimize the effect of any stress that could develop during cold compression. Following this, the temperature was lowered down to 300 K in 200 K steps. At each P-T condition, an X-ray diffraction pattern was collected after the experiment temperature was maintained for ~600 s. The typical exposure time for collecting the diffraction patterns of the sample and the pressure marker was 600 s. Details of the experimental setup and cell assembly are described in Fan et al. (2010).

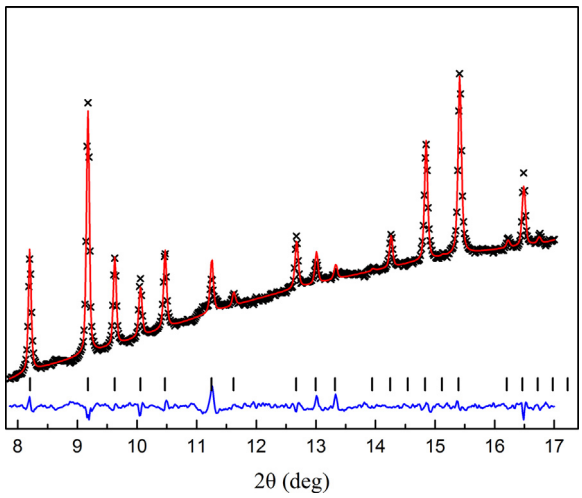

Fig. 2. Le Bail profile fitting of the hydrous pyrope diffraction profiles at 13.21 GPa and 900 K. Observed spectra (*black line*), fitted spectra (*red solid line*), difference plot (*blue solid line*) and Bragg peak positions (*tick marks*) are shown. (For interpretation of the references to colour in this figure legend, the reader is referred to the web version of this article.)

In situ high temperature and high pressure powder X-ray diffraction experiments were conducted at the 4W2 beamline of the Beijing Synchrotron Radiation Facility (BSRF). An image plate detector (MAR-345) was used to collect diffraction patterns. The wavelength of the monochromatic X-ray beam was 0.6199 Å and calibrated by scanning through the Mo metal *K*-absorption edge. The X-ray beam was focused to a beam size of 20 × 30 μm^2 full-width at half maximum (FWHM) by a pair of Kirkpatrick-Baez mirrors. The tilting and rotation of the detector relative to the incident X-ray beam was calibrated using cerium dioxide (CeO_2) powder as the X-ray diffraction standard. The sample-detector distance was calculated from the powder CeO_2 diffraction pattern at ambient conditions. The collected diffraction patterns were integrated to generate the conventional one-dimensional diffraction profiles using Fit2D (Hammersley et al., 1996). Fig. 2 shows a typical fitting of the full X-ray diffraction pattern of hydrous pyrope at 10.79 GPa and 900 K. Analyses of all the patterns were carried out using the full profile-fitting technique implemented in the EXPGUI/GSAS software package (Larson and Von Dreele, 2000; Toby, 2001). The refinement of the peak positions and extraction of the cell parameters were achieved by reducing full diffraction patterns following the Le Bail method (Le Bail et al., 1988). Precision of the volume determination for hydrous pyrope was estimated from the full spectrum fitting (Le Bail refinement) of X-ray diffraction profiles.

3. Results and discussion

The unit-cell parameters of hydrous pyrope refined from single-crystal and powder X-ray diffraction are summarized in Table 1

and 2, respectively. The room temperature and high pressure single-crystal X-ray diffraction data were fitted to the third-order BM-EoS to derive bulk modulus (K_0) and its pressure derivative (K'_0) of hydrous pyrope. For the high temperature and high pressure powder X-ray diffracton data, first we fitted the compression *P-V* data at the 300 K isotherm to the BM-EoS for comparison, and then applied the high-temperature BM-EoS and thermal pressure EoS approach to derive the thermoelastic parameters from the measured *P-V-T* data.

3.1. Room-temperature Birch-Murnaghan equation of state (BM-EoS)

The pressure-volume (*P-V*) data from the single-crystal (Table 1) and powder sample (Table 2) were fitted to a third order BM-EoS:

$$P = (3/2)\ K_0\ [(V_0/V)^{7/3} - (V_0/V)^{5/3}] \times \{1 + (3/4)(K'_0 - 4) \times [(V_0/V)^{2/3} - 1]\} \quad (1)$$

where V_0, K_0, and K'_0 are the unit-cell volume, isothermal bulk modulus and its pressure derivative at ambient conditions, respectively. The fitting without any constraints yielded $V_0 = 1505.14 \pm 0.38$ Å^3, $K_0 = 160 \pm 3$ GPa, $K'_0 = 5.2 \pm 0.4$ for the single-crystal sample and $V_0 = 1505.35 \pm 0.25$ Å^3, $K_0 = 161 \pm 2$ GPa, $K'_0 = 5.0 \pm 0.3$ for the powder sample. With fixed K'_0 at 4 (*i.e.* the second order BM-EoS), the fitting yielded $V_0 = 1504.58 \pm 0.32$ Å^3 and $K_0 = 166 \pm 2$ GPa for the single-crystal and $V_0 = 1505.04 \pm 0.29$ Å^3 and $K_0 = 167 \pm 1$ GPa for the powder. The single-crystal and powder data show excellent agreement with each other. Fitting the combined data yielded: $V_0 = 1505.02 \pm 0.23$ Å^3, $K_0 = 161 \pm 2$ GPa, $K'_0 = 5.2 \pm 0.3$ (without any constraints) and $V_0 = 1504.33 \pm 0.31$ Å^3, and $K_0 = 167 \pm 1$ GPa (with fixed $K'_0 = 4$). Fig. 3 shows the volume compression (V/V_0) of hydrous pyrope as a function of pressure (P) and the derived equation of state from the combined data (without any constraints). From Fig. 3, we can also see that the volume compressions of hydrous pyrope are consistent before and after heating (Table 2). In addition, although the water content was difficult to determine after the high-pressure and temperature powder X-ray diffraction measurements of the hydrous pyrope sample in this study, Dai et al. (2012) determined the water content before and after measurements of the electrical conductivity of hydrous garnet, indicating a water loss of less than 10%. The pressure range in this study (~15 GPa) is significantly higher than Dai et al. (2012) (~4 GPa), while the temperature range in this study (~900 K) is obviously lower than Dai et al. (2012) (~1273 K). Therefore, we infer that there was no obvious water loss during the experimental pressure-temperature range in this study.

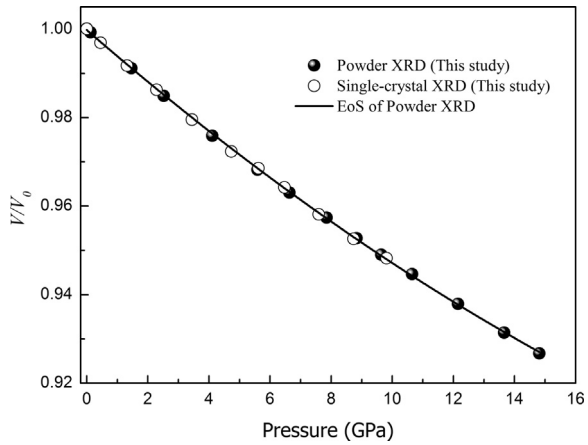

Fig. 3. Volume compression of hydrous pyrope at high pressure and room temperature from single-crystal X-ray diffraction experiments compared with the powder X-ray diffraction experiments in this study. The third-order BM EoS fitted with K_0 and K'_0 are 161 GPa and 5.0 for hydrous pyrope. The error bars of the data points are smaller than the symbols.

The second order BM-EoS yielded a significant larger K_0 than the third order BM-EoS. Fig. 4 shows the volume Eulerian finite strain ($f_E = [(V_0/V)^{2/3} - 1]$) versus the "normalized pressure" ($F_E = P/[3f_E(2f_E + 1)^{5/2}]$) plot (*i.e.* $F_E - f_E$ plot, (Angel, 2000)) of hydrous pyrope in this study. The weighted linear regression through the data points yielded the hydrous pyrope intercept value, $F_E(0) = 161 \pm 2$ GPa, which shows excellent agreement with the isothermal bulk modulus obtained by the third-order BM-EoS (161 ± 2 GPa). Furthermore, it is clear from Fig. 4 that the normalized pressure as a function of the Eulerian strain at 300 K has a positive slope, which is consistent with a value of K'_0 slightly larger than 4 (Angel, 2000) shows that the third-order BM-EoS is a reasonable description of the *P-V* data in this study (see Fig. 5).

We used a methanol-ethanol mixture with a ratio of 4:1 for the pressure medium in this study. This medium solidifies at a pressure above 10 GPa, and therefore the hydrostatic pressure environment in the sample chamber may be influenced (Piermarini et al., 1973; Angel et al., 2007). However, the sample chamber in this study was heated up to 900 K at pressures higher than 10 GPa for the relaxation of the deviatoric stress. The effect of deviatoric stress on the unit-cell volume measurements should be minimal, and this is confirmed by fitting the experimental data under hydrostatic conditions (below 10 GPa) which yields a very similar result ($K_0 = 162 \pm 3$ GPa, $K'_0 = 4.9 \pm 0.5$) to the whole pressure range fitting.

Table 2
Unit cell parameters of hydrous pyrope from powder X-ray diffraction data at various pressure-temperature conditions.

P (GPa)	T (K)	V (Å^3)	P (GPa)	T (K)	V (Å^3)
Compression before heating			9.38(58)	500	1438.79(83)
0.0	300	1505.53(64)	11.28(66)	500	1425.85(75)
1.46(22)	300	1492.13(76)	13.44(54)	500	1410.82(78)
5.59(51)	300	1457.56(86)	15.26(62)	500	1399.73(85)
7.85(37)	300	1441.26(82)	2.46(54)	700	1501.16(86)
9.64(48)	300	1428.62(85)	4.52(59)	700	1484.16(78)
Compression after heating			6.77(33)	700	1466.09(86)
0.12(1)	300	1504.28(92)	8.45(45)	700	1453.06(92)
2.52(32)	300	1482.26(85)	10.28(52)	700	1439.25(81)
4.11(47)	300	1469.09(84)	12.49(54)	700	1424.36(76)
6.63(57)	300	1449.75(74)	14.55(63)	700	1411.26(79)
8.83(63)	300	1434.26(87)	16.03(47)	700	1402.62(84)
10.65(58)	300	1422.08(84)	2.98(56)	900	1506.36(77)
12.15(55)	300	1411.87(88)	5.33(46)	900	1486.09(83)
13.66(28)	300	1402.09(75)	7.42(58)	900	1469.75(84)
14.81(37)	300	1395.10(92)	9.37(52)	900	1454.95(77)
1.55(15)	500	1500.13(86)	10.79(45)	900	1444.35(83)
3.28(24)	500	1484.66(83)	13.21(36)	900	1427.76(78)
5.44(33)	500	1467.09(87)	15.44(45)	900	1413.76(82)
7.56(45)	500	1450.83(76)	16.75(64)	900	1406.12(87)

Numbers in parenthesis represent standard deviations.

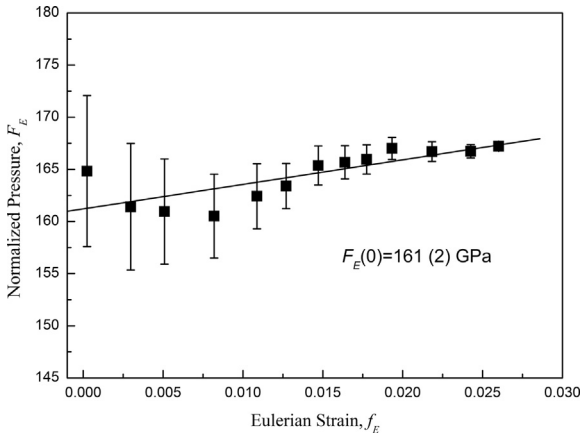

Fig. 4. Volume Eulerian strain-normalized pressure (F_E-f_E) plot of hydrous pyrope. The solid line represents the linear fit through the data.

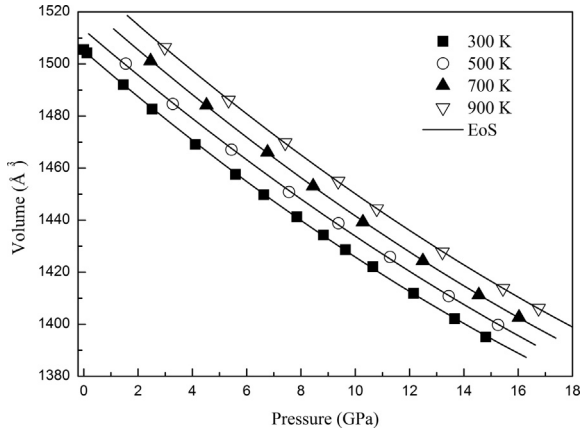

Fig. 5. Unit-cell volume of hydrous pyrope as a function of pressure and temperature. The solid lines represent the isothermal compression curve from fitting the HTBM EoS at 300, 500, 700, 900 K with the following parameters: K_0 = 162 ± 1 GPa, K'_0 = 4.9 ± 0.2, $(\partial K_0/\partial T)_P$ = −0.018 ± 0.004 GPa K^{-1} and α_0 = (3.19 ± 0.10) × 10^{-5} K^{-1}. The error bars of the data points are smaller than the symbols.

3.2. High-temperature Birch-Murnaghan equation of state

The *P-V-T* data (Table 2) from powder X-ray diffraction experiments were used to determine the thermoelastic properties of hydrous pyrope up to ~17 GPa and 900 K. The high temperature third order BM-EoS was applied to our high pressure and high temperature data in the following form:

$$P = (3/2)\ K_{T0}\ [(V_{T0}/V)^{7/3} - (V_{T0}/V)^{5/3}] \times \{1 + (3/4)(K'_{T0} - 4) \times [(V_{T0}/V)^{2/3} - 1]\} \quad (2)$$

In this equation, the thermal dependences of the zero-pressure volume (V_{T0}) and the bulk modulus (K_{T0}) at different temperatures are expressed using the following equations:

$$V_{T0} = V_0 \exp \int_{300}^{T} \alpha_T dT \quad (3)$$

$$KT0 = K0 + (\partial K0/\partial T)P \times (T - 300) \quad (4)$$

where α_T is the thermal expansion at ambient pressure and $(\partial K_0/\partial T)_P$ is the temperature derivative of K_0 at ambient pressure.

The hydrous pyrope thermoelastic parameters obtained in this study are shown in Table 4. Fitting our *P-V-T* data to the high temperature BM EoS yielded V_0 = 1505.38 ± 0.27 Å^3, K_0 = 162 ± 1 GPa, K'_0 = 4.9 ± 0.2, $(\partial K_0/\partial T)_P$ = −0.018 ± 0.004 GPa K^{-1} and α_0 =(3.2 ± 0.1)×10^{-5} K^{-1}. With K'_0 fixed to 4.0, we also obtained V_0 = 1505.22 ± 0.28 Å^3, K_0 = 168 ± 1 GPa, $(\partial K_0/\partial T)_P$ = −0.017 ± 0.005 GPa K^{-1} and α_0 = (3.06 ± 0.09)× 10^{-5} K^{-1} for hydrous pyrope. The K_0 values determined here are consistent with those derived from our *P-V* data fitting at 300 K within accepted uncertainties. We also calculated the temperature derivative of the bulk modulus extracted from each isotherm, and obtained $(\partial K_0/\partial T)_P$ = −0.018 ± 0.005 GPa K^{-1} for hydrous pyrope, which is very consistent with the results from the whole set of *P-V-T* data available in this study ($(\partial K_0/\partial T)_P$ = −0.018 ± 0.004 GPa K^{-1}) within their uncertainties.

Likewise, fitting the *P-V-T* data at pressures below ~10 GPa to the high temperature BM-EoS yielded V_0 = 1505.33 ± 0.31 Å^3, K_0 = 163 ± 2 GPa, K'_0 = 5.1 ± 0.4, $(\partial K_0/\partial T)_P$ = −0.020 ± 0.006 GPa K^{-1} and α_0 = (3.3 ± 0.2)×10^{-5} K^{-1}. These values are very consistent with all the *P-V-T* data fitting results within their uncertainties.

3.3. Thermal pressure equation of state

We also analyzed the *P-V-T* data using a thermal pressure approach (e.g., Anderson, 1995; Jackson and Rigden, 1996). The thermal pressure (ΔPth) was obtained by subtracting the pressure at volume (V) and at room temperature (derived from Eq. (1)) from the pressure measured at the same V and at temperature (T).

$$\Delta P\text{th} = P(V,T) - P(V,300) = \left[\alpha K_T + \left(\frac{\partial K_T}{\partial T}\right)_V \ln\left(\frac{V_0}{V}\right)\right] \times (T - 300) \quad (5)$$

Figs. 6 and 7 show the thermal pressure of hydrous pyrope against temperature and the unit-cell volume, respectively. These data show that the thermal pressure of hydrous pyrope varies linearly with temperature and is almost independent of volume. Therefore, we assume that $(\partial K_T/\partial T)_V = 0$ so the thermal pressures in Eq. (5) are independent of volume, an approximation that has been derived or assumed in many previous studies for mantle phases (e.g., Guyot et al., 1996; Wang et al., 1996, 1998; Anderson, 1999; Shim et al., 2000; Nishihara et al., 2004; Liu and Li, 2006; Liu et al., 2008; Fan et al., 2015). With this assumption, fitting the data in this study yielded K_0 = 160 ± 2 GPa, K'_0 = 4.8 ± 0.4, and α_0 = (2.9 ± 0.2)×10^{-5} K^{-1}, which is reasonably consistent with those derived by the HTBM EoS fitting (Table 4). By using the thermodynamic relation: $(\partial K_T/\partial T)_P = (\partial K_T/\partial T)_V - \alpha K_T\ K'_T$, we obtained $(\partial K_0/\partial T)_P$ = −0.021(3) GPa K^{-1}, which is in good agreement with current analysis using the HTBM EoS (Table 4).

3.4. Comparison with previous studies of other garnets

Our hydrous pyrope results compared with previous studies for anhydrous pyrope are also shown in Table 3. Numerous studies on elastic properties of anhydrous pyrope have been investigated by some authors. Table 3 summarizes the V_0, K_0 and K'_0 for anhydrous pyrope determined by various experimental techniques, including X-ray diffraction, ultrasonic interferometry and Brillouin scattering spectroscopy (Hazen and Finger, 1978; Sato et al., 1978; Levien et al., 1979; Leitner et al., 1980; Leger et al., 1990; Conrad et al., 1999; Zhang et al., 1998; Chen et al., 1999; Wang and Ji, 2001; Sinogeikin and Bass, 2000, 2002a,b; Li et al., 2011; Du et al., 2015). We observed a systematic expansion of the zero-pressure unit-cell volume with hydration at ambient conditions from Tables 3 and 4, which is in good agreement with many previous studies for other mantle minerals (e.g., Smyth et al., 2003; Smyth and Jacobsen, 2006; Holl et al., 2008; Ye et al., 2010, 2012). In addition, Fig. 8 shows the difference between the unit-cell volumes of the anhydrous and hydrous pyropes as a function of pressure. The anhydrous reference volume chosen for comparison in Fig. 8 was from Du et al. (2015), because they used the same pressure transmitting medium (4:1 methanol-ethanol mixture) and had a similar pressure range with this study. From Fig. 8, we see the unit-cell volumes of the anhydrous pyrope are slightly smaller than hydrous pyrope in this study at low pressures, while their unit-cell volumes become very close to each other at higher pressures due to the larger compressibility (smaller bulk modulus) of the hydrous sample. Levien et al. (1979) measured the unit-cell parameters of pyrope in a diamond anvil cell at pressures up to 5 GPa using a single crystal X-

Table 3
Bulk modulus and its pressure derivative of dry pyrope and hydrous pyrope.

Sample	K_0 (GPa)	K'_0	V_0 (Å^3)	Methods	References
Hydrous pyrope	167(1)	4.0[a]	1505.04(29)	Powder-XRD	This study
Hydrous pyrope	161(2)	5.0(3)	1505.35(25)	Powder-XRD	This study
Hydrous pyrope	166(2)	4.0[a]	1504.58(32)	Single crystal-XRD	This study
Hydrous pyrope	160(3)	5.2(4)	1505.14(38)	Single crystal-XRD	This study
Dry pyrope	172.8	3.8(1)	1503.87	Powder-XRD	Leger et al. (1990)
Dry pyrope	169.2(2)	4.4[a]	1503.2	Powder-XRD	Du et al. (2015)
Dry pyrope	175(1)	4.5(5)	1503.4(5)	Single crystal-XRD	Levien et al. (1979)
Dry pyrope	171(2)	4.4(2)	1502.9(3)	Single crystal-XRD	Zhang et al. (1998)
Dry pyrope	171.32(2)	3.22	–	BLS	Conrad et al. (1999)
Dry pyrope	171.2(20)	4.1(3)	–	BLS	Sinogeikin and Bass (2000)
Dry pyrope	174.9(16)	4.7(3)	–	BLS	Jiang et al. (2004)
Dry pyrope	171(2)	5.3(4)	–	UI	Chen et al. (1999)
Dry pyrope	170.1(11)	4.9(6)	–	UI	Wang and Ji (2001)

XRD, X-ray diffraction; BS, Brillouin Light Scattering; UI, Ultrosonic interferometry.
Numbers in parenthesis represent standard deviations.
[a] Fixed during fitting.

Table 4
Thermoelastic parameters of hydrous pyrope using the HTBM equation of state compared with dry pyrope.

Sample	V_0 (Å^3)	K_0 (GPa)	K'_0	$(\partial K/\partial T)_P$ (GPa K^{-1})	α_0 (10^{-5} K^{-1})	References
Dry pyrope	1503.1(5)	170(2)	5.0[a]	−0.020(3)	2.58(28)	Wang et al. (1998)
Dry pyrope	–	169(2)	–	−0.019(3)	–	Sinogeikin and Bass (2002)
Dry pyrope	1502.5	172(4)	3.9[a]	−0.026(2)	–	Gwanmesia et al. (2006)
Dry pyrope	1500.4(15)	167(3)	4.6[a]	−0.021(9)	2.89(33)	Zou et al. (2012)
Dry pyrope	1502.8(4)	–	–	–	2.74(5)	Du et al. (2015)
Hydrous pyrope	1505.38(27)	162(1)	4.9(2)	−0.018(4)	3.19(10)	This study
Hydrous pyrope	1505.22(28)	168(1)	4.0[a]	−0.017(5)	3.06(9)	This study

Numbers in parenthesis represent standard deviations.
[a] Fixed during fitting.

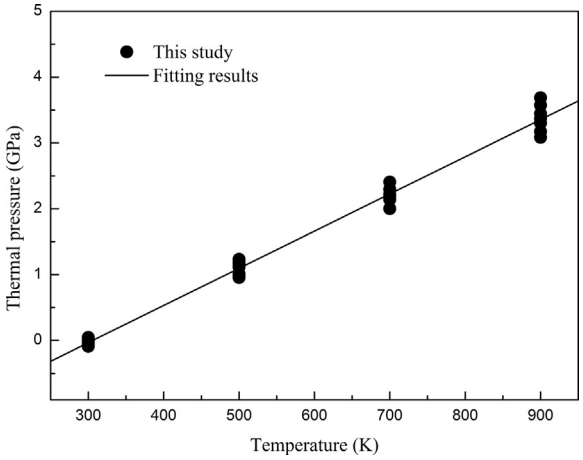

Fig. 6. Thermal pressure of hydrous pyrope verses temperature. Solid circles are the hydrous pyrope data in this study. The solid line is the fitting results using a thermal pressure approach.

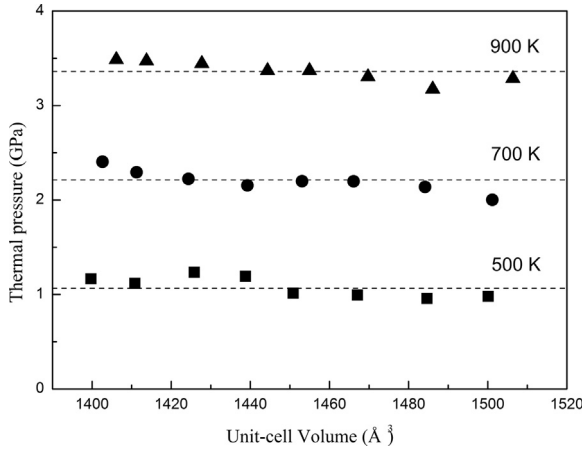

Fig. 7. Variations of thermal pressure with the unit-cell volume at various temperatures. The dashed lines correspond to the constant values of thermal pressure for a given temperature. The data indicates that $(\partial K_T/\partial T)_V$ is close to zero.

ray diffraction method, and obtained the bulk modulus K_0 = 175(1) GPa and K'_0 = 4.5(5). Leitner et al. (1980) determined the elastic moduli of a synthetic single crystal of pyrope using Brillouin spectroscopy, and reported K_0 = 175(1) GPa. Subsequently, Leger et al. (1990) used this K_0 value and using powder X-ray diffraction to report K'_0 = 3.4 for pure synthetic pryope. Zhang et al. (1998) also investigated the equation of state and crystal structure of pyrope under hydrostatic conditions up to 33 GPa using single crystal X-ray diffraction, and obtained K_0 = 171(2) GPa and K'_0 = 4.4(2). In addition, Conrad et al. (1999) conducted high-pressure Brillouin scattering experiments on near end-member single crystal pyrope at pressures up to 10 GPa in a diamond-anvil cell with a methanol-ethanol-water pressure medium, and calculated K_0 and K'_0 as 171.3 GPa and 3.22, respectively. Sinogeikin and Bass (2000) also measured the single-crystal elastic properties of synthetic pyrope up to 20 GPa using a Brillouin scattering method, and reported that the K_0 and K'_0 were 169.4(20) GPa and 4.1(3), respectively. In contrast, studies using synthetic polycrystalline specimens and ultrasonic interferometry in a 1000 ton split-cylinder multi-anvil apparatus (Chen et al., 1999) yielded K_0 = 171(2) and K'_0 = 5.3(4), the largest value of K'_0 in the previous studies for anhydrous pyrope. Recently, Du et al. (2015) also measured the unit-cell parameters of synthetic pyrope up to 10 GPa using synchrotron X-ray powder diffraction, and yielded K_0 = 169.2(2) by fixing K'_0 at 4.4 which taken from Zhang et al. (1998). From the results of these previous studies, the anhydrous pyrope bulk modulus and its pressure derivative are within the ranges of K_0 = 170–175 GPa and K'_0 = 3.2–5.3. However, we obtained the bulk modulus and its pressure derivative as K_0 = 161 GPa and K'_0 = 5.0 for the hydrous pyrope (about 900 ppmw) in this study. The K_0 value of our hydrous pyrope was around 5–7% smaller than the anhydrous pyrope from previous studies, but its K'_0 value was slightly larger. This

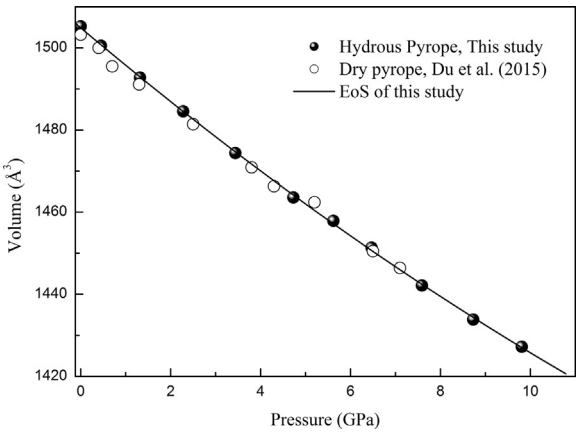

Fig. 8. Unit-cell volumes of anhydrous and hydrous pyrope at ambient temperature with pressures from 0 to about 10 GPa. The third-order BM EoS fitted with K_0 and K'_0 are 160 GPa and 5.2 for hydrous pyrope. The error bars of the data points are smaller than the symbols.

phenomenon is similar to the effects of water on the elastic properties of olivine, reducing K_0 and increasing K'_0 (Smyth et al., 2005; Jacobsen, 2006) although unchanged K'_0 for hydrous olivine was also proposed (Chen et al., 2011).

In addition, as an important garnet end-member, grossular is a promising water carrier mineral in the garnet family (Rossman, 1996). Although Bolfan-Casanova et al. (2000) doubted the hydrogarnet substitution in majorite, based on the IR spectra of synthesized tetragonal $MgSiO_3$ majorite, Pigott et al. (2015) showed that even with low-water contents, the hydrogarnet defect was likely to form in majorite, thus they inferred that majorite also incorporated water mainly through hydrogarnet substitution. Therefore, hydrogen enters the garnet structure mainly through the hydrogarnet substitution of $H_4O_4 = -SiO_4$ (e.g., Lager et al., 2005; Jacobsen, 2006). The hydrogarnet substitution in grossular is expressed as $Ca_3Al_2(SiO_4)_{3-x}(H_4O_4)_x$, named hibschite ($0 < x < 1.5$) and katoite ($1.5 < x \leq 3.0$) (Jacobsen, 2006). A lot of studies on the elastic properties of grossular have been determined by X-ray diffraction, ultrasonic interferometry, and Brillouin scattering spectroscopy (e.g., Bass, 1989; Conrad et al., 1999; Olijnyk et al., 1991; Pavese et al., 2001; Kono et al., 2010; Gréaux et al., 2011), giving K_0 values from 166 to 172 GPa. In addition, the elastic properties of a natural hibschite were determined by Brillouin spectroscopy, giving $K_0 = 99.8$ (10) GPa (O'Neill et al., 1993). The compressibility of katoite was studied by powder (Olijnyk et al., 1991) and single-crystal (Lager et al., 2002) X-ray diffraction experiments, giving $K_0 = 66(4)$ GPa and 58(1) GPa, respectively. Thus, in going from grossular to hibschite and katoite, the bulk moduli were reduced by ~40% and ~60%, respectively. This is also very similar to the effects of water on the elastic properties of the pyrope garnet in this study, although K_0 changed less for hydrous pyrope since there is less water content in pyrope garnet compared with grossular. In other words, the increased compressibility of garnets (e.g. pyrope, grossular) with increasing water is due to the positive volume change by introduction of the H_4O_4 tetrahedron compared with the smaller and more rigid SiO_4 tetrahedron (Jacobsen, 2006).

In order to obtain a consistent thermoelastic parameter set, Wang et al. (1998) refitted the entire data set of pyrope garnet at high pressure and temperature using the data from previous studies (Yagi et al., 1987; Suzuki and Anderson, 1983; and others). By fixing $K'_0 = 5$, they obtained $K_0 = 170(2)$ GPa, $(\partial K_0/\partial T)_P = -0.020(3)$ GPa K^{-1}, and $\alpha_0 = 2.58(28) \times 10^{-5}$ K^{-1}. Sinogeikin and Bass (2002a,b) presented the single-crystal elasticity of pure synthetic pyrope at temperatures up to 800 °C using Brillouin light scattering spectroscopy in a ceramic high-temperature cell, indicating $K_0 = 169(2)$ GPa and $(\partial K_0/\partial T)_P = -0.019(3)$ GPa K^{-1}. Gwanmesia et al. (2006) determined the acoustic wave velocities of synthetic polycrystalline pyrope up to 9 GPa and 1000 °C by ultrasonic interferometry combined with energy-dispersive synchrotron X-ray diffraction in a cubic-anvil DIA-type apparatus, and obtained $K_0 = 172$ (2) GPa and $(\partial K_0/\partial T)_P = -0.026(4)$ GPa K^{-1} by fixing $K'_0 = 3.9$. Recently, Zou et al. (2012) measured the thermoelastic properties of synthetic pyrope garnet at higher pressure and temperature conditions (up to 19 GPa and 1700 K) using *in situ* energy-dispersive synchrotron X-ray diffraction combined with a Kawai-type multi-anvil apparatus, and concluded that $K_0 = 167(3)$ GPa, $(\partial K_0/\partial T)_P = -0.021(9)$ GPa K^{-1}, and $\alpha_0 = 2.89(33) \times 10^{-5}$ K^{-1} for fixed $K'_0 = 4.6$. Du et al. (2015) also investigated the thermo-compression of a series of synthetic garnets with the pyrope, grossular, and intermediate compositions up to about 900 K and to 10 GPa using synchrotron X-ray powder diffraction with a diamond anvil cell, and obtained $\alpha_0 = 2.74(5) \times 10^{-5}$ K^{-1} for end-member pyrope. The results of previous studies indicate that the temperature derivative of anhydrous pyrope bulk modulus ($(\partial K_0/\partial T)_P$) ranges from −0.019 GPa K^{-1} to −0.026 GPa K^{-1}, and the coefficients of thermal expansion (α_0) range from 2.58×10^{-5} K^{-1} to 2.89×10^{-5} K^{-1}. However, we obtained $(\partial K_0/\partial T)_P = -0.018(4)$ GPa K^{-1} and $\alpha_0 = 3.2(1) \times 10^{-5}$ K^{-1} for hydrous pyrope (about 900 ppmw) in this study. The $(\partial K/\partial T)_P$ value of the hydrous pyrope in this study is in agreement with anhydrous pyrope, whereas the α_0 value of the hydrous pyrope is slightly larger than anhydrous pyrope. Lu et al. (2013) measured the single-crystal elasticity of natural Fe-bearing pyrope using *in situ* Brillouin spectroscopy and X-ray diffraction at high-pressure and temperature conditions up to 20 GPa and 750 K in an externally-heated diamond anvil cell, and found $(\partial K_0/\partial T)_P = -0.023(2)$ GPa K^{-1} for Fe-bearing pyrope, which is very consistent with the results from Wang et al. (1998) ($(\partial K_0/\partial T)_P = -0.020(3)$ GPa K^{-1}) and Zou et al. (2012) ($(\partial K_0/\partial T)_P = -0.021(9)$ GPa K^{-1}) for pure pyrope using a synchrotron X-ray diffraction method within their uncertainties. Therefore, based on the existing data, we believe that the temperature derivative of the pyrope bulk modulus may not be significantly affected by its iron and hydrogen content; however, hydrogen can slightly raise the thermal expansion coefficient of pyrope.

4. Geophysical implications

Earth's mantle mostly consists of nominally anhydrous minerals, such as olivine, pyroxenes, garnet, and their high-pressure equivalents (Williams and Hemley, 2001). Although these minerals do not contain OH groups in their formulas, they can dissolve traces of OH as point defects (Hirschmann, 2006). Investigations of natural samples suggest that these minerals may represent a major reservoir of water in the Earth (e.g. Rossman and Smyth, 1990; Skogby et al., 1990; Smyth et al., 1991; Bell and Rossman, 1992a, 1992b; Rossman, 1996; Bell et al., 2003). Pyrope occurs commonly in nature both as a metamorphic mineral and as a high-pressure phase, which is stable under upper mantle conditions (Leitner et al., 1980), and it is probably also important in the mantle-transition zone (420–670 km) depth phases (Duffy and Anderson, 1989). Furthermore, previous studies also predicted that pyrope could incorporate significant amounts of water as hydroxyl (e.g. Bell and Rossman, 1992b; Bell et al., 1995; Beran and Libowitzky, 2006). Therefore, using the newly-determined thermoelastic properties of hydrous pyrope in our present study, we calculated the density profiles of the major upper-mantle minerals.

We used the high-temperature BM-EoS to calculate the densities of the following constituent minerals at conditions corresponding to the upper mantle: pure olivine (Mg_2SiO_4) (Guyot et al., 1996) and Fe-bearing olivine ($(Mg_{0.9}Fe_{0.1})_2SiO_4$) (Liu and Li, 2006)), pure orthopyroxene (*Pbca*, $MgSiO_3$) (Zhao et al., 1995), pure orthopyroxene (*C2/c*, $MgSiO_3$) (Shinmei et al., 1999), pure clinopyroxene ($CaMgSi_2O_6$) (Zhao et al., 1998) and Fe-bearing clinopyroxene (omphacite-$Di_{63}Jd_{37}$; Di = Ca(Mg, Fe)Si_2O_6, Jd = $NaAlSi_2O_6$) (Nishihara et al., 2003), pure pyrope ($Mg_3Al_2Si_3O_{12}$) (Zou et al., 2012) and Fe-bearing pyrope ($(Mg_{0.83}Fe_{0.17})_3Al_2Si_3O_{12}$) (Suzuki and Anderson, 1983; Lu et al., 2013; Huang and Chen, 2014), and hydrous pure pyrope ($Mg_3Al_2Si_3O_{12}$) (this study). As shown in previous studies, orthopyroxene with the space group *Pbca* transforms to high-pressure *C2/c* clinoenstatite at the relevant pressure and temperature conditions of the upper mantle (e.g. Shinmei et al., 1999; Bromiley and Bromiley, 2006; Yu and Wentzcovitch, 2009; Finkelstein et al., 2015), and we assumed that the OEN phase (*Pbca*) transitions into the HP-CEN phase (*C2/c*) at 250 km (~8 GPa). Therefore, we used the thermoelastic parameters of *C2/c* clinoenstatite by Shinmei et al. (1999) for pressures higher than 8 GPa, and *Pbca* orthopyroxene by Zhao et al. (1995) for pressures lower than 8 GPa in our calculations. In addition, the effect of iron incorporation on the thermoelastic properties of orthopyroxene (*Pbca* phase) was studied experimentally (Zhang et al., 2013). They indicated that incorporation of a small

amount of iron (about 13% ferrosilite content) in enstatite just increases the pressure derivative of the bulk modulus from about 10 to 13, but has a negligible effect on other thermoelastic parameters (Zhao et al., 1995; Zhang et al., 2013). Moreover, there is still a lack of related detailed experimental studies about the effect of iron incorporation on the thermoelastic properties of orthopyroxene (*C2/c* phase). Thus in our calculations, we assumed that the incorporation of a small amount of iron has a negligible effect on the thermoelastic properties of orthopyroxene (*Pbca* and *C2/c* phases).

Fig. 9 shows the density-profiles of the constituent minerals for the Earth's upper mantle region between a 200 and 400 km depth along a normal continental geotherm (Katsura et al., 2010). The PREM density-profile (Dziewonski and Anderson, 1981) is also shown in Fig. 9 for comparison. Compared with the modeled densities of anhydrous pure pyrope (Zou et al., 2012) at the P-T conditions of the upper mantle, our results show that the hydrogen effect on thermoelasticity of pyrope leads to a ~1% decrease in the density. In addition, since the temperature range (~900 K) in the present P-V-T experiments was limited, the thermal expansion coefficient at zero-pressure was treated as a constant in the P-V-T data analysis of hydrous pyrope. This factor may lead to uncertainty in the extrapolated density profile of hydrous pyrope in the Earth's upper mantle region. Therefore, we needed to assess the possible uncertainties of the density profile of the hydrous pyrope in this study. First, we determined the temperature dependence of the thermal expansion coefficient of hydrous pyrope using the P-V-T data in this study, which yielded $V_0 = 1505.13 \pm 0.25$ Å^3, $K_0 = 162 \pm 1$ GPa, $K'_0 = 5.0 \pm 0.2$, $(\partial K_0/\partial T)_P = -0.014 \pm 0.002$ GPa K^{-1} and $\alpha_0 = (2.87 \pm 0.13)\times10^{-5}$ K^{-1}, and $\alpha_1 = (0.61 \pm 0.22)\times10^{-8}$ K^{-1}. Using these results, we also calculated the density profile of hydrous pyrope, which shows a higher density of just ~0.15%. Second, in consideration of the very minimal effect of hydrogen on the thermal expansion coefficient at ambient conditions of pyrope (Table 4), we used the thermal expansion coefficient of dry pure pyrope ($\alpha_0 = (2.58 \pm 0.20) \times 10^{-5}$ K^{-1}, and $\alpha_1 = (1.02 \pm 0.46)\times10^{-8}$ K^{-1}) (Zou et al., 2012) to calculate the density profile of hydrous pyrope. The resulting density profile also shows just ~0.2% higher density. To sum up, we infer that if the thermal expansion coefficient at zero-pressure is treated as a constant in the P-V-T data analysis of hydrous pyrope, it may lead to very limited uncertainty in the extrapolated density profile of hydrous pyrope in the Earth's upper mantle region.

Furthermore, the density profiles of olivine, orthopyroxene, and clinopyroxene were also modeled using existing results on their thermoelasticity parameters (Suzuki and Anderson, 1983; Guyot et al., 1996; Zhao et al., 1995, 1998; Shinmei et al., 1999; Nishihara et al., 2003; Liu and Li, 2006; Lu et al., 2013; Huang and Chen, 2014). The density profile of hydrous pure pyrope was ~4% higher than the PREM density profile, but closer to the PREM than the anhydrous pure pyrope (~5% higher) and Fe-bearing pyrope (~6.5% higher) density profile. Furthermore, the density profile of pure olivine and pure Cpx was ~3% and ~2% lower than the PREM density profile, respectively, whereas the density profiles of Fe-bearing olivine and Fe-bearing Cpx were very close to the PREM density profile. In conclusion, the density profiles of the upper mantle minerals at the relevant P-T conditions are highly dependent on their iron content. Based on the phase diagram of Opx (Woodland, 1998), we assume that the Opx phase (*Pbca*) transitions into the HP-Cpx phase (*C2/c*) at 250 km (~8 GPa) and is accompanied by a density jump, where the density profile of pure Opx is ~1.5% lower than the PREM density profile at depths up 250 km, whereas the density profile of pure Opx is ~1.5% higher than the PREM density profile at depths under 250 km.

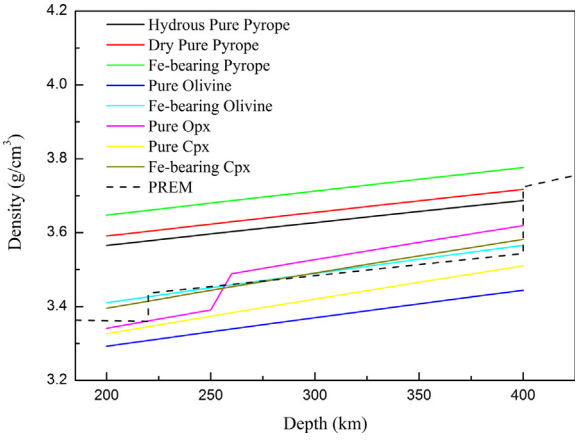

Fig. 9. Calculated density profiles of constituent minerals in the upper mantle between 200 and 400 km. Anhydrous pyrope (red solid line) (Zou et al., 2012), Hydrous pyrope (black solid line) (This study), Fe-bearing pyrope (green solid line) (Suzuki and Anderson, 1983; Lu et al., 2013; Huang and Chen, 2014), pure Olivine (blue solid line) (Guyot et al., 1996), Fe-bearing Olivine (cyan solid line) (Liu and Li, 2006), pure Opx (magenta solid line) (Zhao et al., 1995; Shinmei et al., 1999), pure Cpx (yellow solid line) (Zhao et al., 1998), and Fe-bearing Cpx (dark yellow solid line) (Nishihara et al., 2003). The PREM density profile is also shown (dashed line). (For interpretation of the references to colour in this figure legend, the reader is referred to the web version of this article.)

To understand the density profiles and mineralogical models of the upper mantle better, we also modeled the density profiles of the representative upper-mantle mineral assemblages-pyrolite, using the updated thermoelastic properties of hydrous pyrope for the Earth's upper mantle region between 200 and 400 km depth (Fig. 10). The pyrolite model represents the global mineral compositions of the upper mantle that are commonly used for comparison between mineral physics results and global density profiles (Lu et al., 2013). The mineral assemblage in pyrolite model includes ~63% olivine, ~15% garnet, ~16% clinopyroxene, and ~6% orthopyroxene (Ita and Stixrude, 1992). Here, we made two assumptions: first, the chemical compositions of the constituent minerals do not change in this P-T range, which results in constant zero-pressure densities of the constituent minerals; and second, the volume proportions of the constituent minerals of pyrolite model are constant. The results are shown in Fig. 10, and the PREM density profile is also shown in this figure for comparison. Fig. 10 shows the density profiles of pyrolite with hydrous pyrope and other pure minerals, and pyrolite with anhydrous pyrope and other pure minerals at Earth's upper mantle region between a 200 and 400 km depth. The density profile of pyrolite with hydrous pyrope and other pure minerals is slightly lower than pyrolite with anhydrous pyrope and other pure minerals, which show that hydrogen in pyrope can decrease the density of the pyrolite model. However, according to the "pyrolite" model, the chemistry of the upper mantle minerals should contain certain components of Fe (Ringwood, 1975). Thus, Fig. 10 also shows that the pyrolite model with all Fe-bearing minerals and the pyrolite model with hydrous pyrope and other Fe-bearing minerals, using the Fe-bearing minerals from Fig. 9. From Fig. 10, the pyrolite model with all Fe-bearing minerals shows the largest density profile; whereas using the hydrous pyrope instead of the anhydrous Fe-bearing pyrope meant the modeled pyrolite with hydrous pyrope and other Fe-bearing minerals showed a lower density profile than the pyrolite model with all Fe-bearing minerals towards the PREM density profile (Fig. 10). Furthermore, considering that the volume proportion of pyrope in the pyrolite model is relatively small compared with olivine and pyroxene, incorporating water into the olivine and pyroxene of the upper mantle may make the density profiles of the pyrolite model match the PREM density profile well. This once again

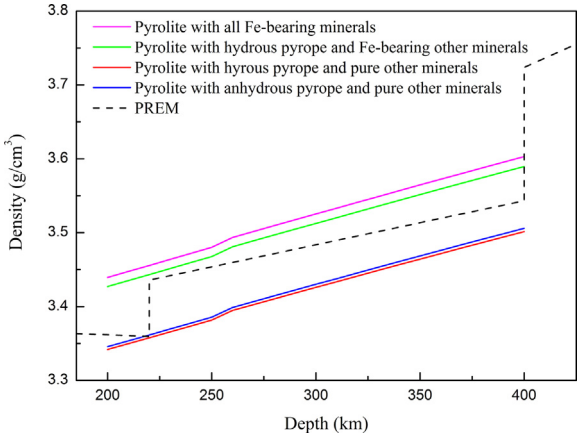

Fig. 10. Calculated density profiles of the pyrolite model. In these calculations, the zero-pressure densities and mineral proportions of the constituent minerals are assumed to be constant. The PREM density profile is also shown (dashed line).

proves that the nominally anhydrous mineral phases in the Earth's upper mantle (olivine, pyroxene, and garnet) can contain a significant amount of hydrogen. However, this still needs to be confirmed by measuring the thermoelasticity of all major hydrous upper mantle minerals (Fe-bearing) at relevant P-T conditions in future experiments.

5. Conclusions

Incorporating 900 ppmw of water in pyrope crystal yields a reduction in its bulk modulus of 7%, a slight increase in its bulk modulus pressure derivative and thermal expansion coefficient, but little change in its bulk modulus temperature derivative. The presence of water in pyrope helps to reduce the densities of the pyrolite model to better match the density profile of the PREM. Incorporating water in olivine and pyroxene is favorable for reconciling the discrepancy in the density profiles between the mineral physics models and the seismological model (PREM).

Acknowledgments

We thank the two anonymous reviewers for their valuable comments and advices which helped to improve the manuscript. D. W. Fan acknowledges financial support from the National Natural Science Foundation of China (41374107), and the Joint Research Fund in Huge Scientific Equipment (U1632112) under cooperative agreement between the National Natural Science Foundation of China and Chinese Academy of Sciences. J. H. Chen acknowledges financial support from the National Science Foundation of US (EAR-1015509). J. G. Xu acknowledges financial support from the Strategic Priority Research Program (B) of the Chinese Academy of Sciences (XDB18010401) . This work was partially supported by the National Natural Science Foundation of China (Grant No. U1530402). The high-temperature and high-pressure powder X-ray diffraction experiments were performed at the High Pressure Experiment Station (4W2), Beijing Synchrotron Radiation Facility (BSRF). The room-temperature and high-pressure single crystal X-ray diffraction experiments were performed at the BL15U1 of the Shanghai Synchrotron Radiation Facility (SSRF).

References

Aines, R.D., Rossman, G.R., 1984. Water in minerals? A peak in the infrared. J. Geophys. Res. 89, 4059–4071.
Akaogi, M., Akimoto, S., 1977. Pyroxene-garnet solid-solution equilibria in the systems $Mg_4Si_4O_{12}$-$Mg_3Al_2Si_3O_{12}$ and $Fe_4Si_4O_{12}$-$Fe_3Al_2Si_3O_{12}$ at high pressures and temperatures. Phys. Earth Planet. Inter. 15, 90–106.
Anderson, O.L., 1995. Equation of State of Solids for Geophysics and Ceramic Science. Oxford University Press, New York, pp. 243–274.
Anderson, O.L., 1999. The volume dependence of thermal pressure in perovskite and other minerals. Phys. Earth Planet. Inter. 112, 267–283.
Anderson, D.L., Bass, J., 1984. Mineralogy and composition of the upper mantle. Geophys. Res. Lett. 11, 637–640.
Angel, R.J., 2000. Equation of state. Rev. Mineral. Geochem. 41, 35–60.
Angel, R.J., Bujak, M., Zhao, J., Gatta, G.D., Jacobsen, S.D., 2007. Effective hydrostatic limits of pressure media for high-pressure crystallographic studies. J. Appl. Crystallogr. 40, 26–32.
Bass, J.D., 1989. Elasticity of grossular and spessartite garnets by Brillouin spectroscopy. J. Geophys. Res. 94, 7621–7628.
Bell, D.R., Rossman, G.R., 1992a. Water in Earth's mantle: the role of nominally anhydrous minerals. Science 255, 1391–1397.
Bell, D.R., Rossman, G.R., 1992b. The distribution of hydroxyl in garnets from the subcontinental mantle of southern Africa. Contrib. Min. Petrol. 111, 161–178.
Bell, D.R., Ihinger, P.D., Rossman, G.R., 1995. Quantitative analysis of trace OH in garnet and pyroxenes. Am. Mineral. 80, 465–474.
Bell, D.R., Rossman, G.R., Maldener, J., Endisch, D., Rauch, F., 2003. Hydroxide in olivine: a quantitative determination of the absolute amount and calibration of the IR spectrum. J. Geophys. Res. 108, 2105.
Beran, A., Libowitzky, E., 2006. Water in natural mantle minerals II: olivine, garnet and accessory Minerals. Rev. Mineral. Geochem. 62, 169–191.
Bolfan-Casanova, N., Keppler, H., Rubie, D.C., 2000. Water partitioning between nominally anhydrous minerals in the MgO-SiO_2-H_2O system up to 24 GPa: implications for the distribution of water in the Earth's mantle. Earth Planet. Sci. Lett. 182, 209–221.
Bonczar, L.J., Graham, E.K., 1977. The pressure and temperature dependence of the elastic constants of pyrope garnet. J. Geophys. Res. 82, 2529–2534.
Boyd, F.R., Pearson, D.G., Hoal, K.O., Hoal, B.G., Nixon, P.H., Kingston, M.J., Mertzman, S.A., 2004. Garnet lherzolites from Louwrensia, Namibia: bulk composition and P/T relations. Lithos 77, 573–592.
Bromiley, G.D., Bromiley, F.A., 2006. High-pressure phase transitions and hydrogen incorporation into $MgSiO_3$ enstatite. Am. Mineral. 91, 1094–1101.
Chen, J., Inoue, T., Weidner, D.J., Wu, Y., Vaughan, M.T., 1998. Strength and Water Weakening of Mantle Minerals, Olivine, Wadsleyite and Ringwoodite. Geophys. Res. Lett. 25. 575–578 & 1103–1104.
Chen, G., Cooke, J.A.J., Gwanmesia, G.D., Liebermann, R.C., 1999. Elastic wave velocities of $Mg_3Al_2Si_3O_{12}$-pyrope garnet to 10 GPa. Am. Mineral. 84, 384–388.
Chen, J., Liu, H., Girard, J., 2011. Comparative in situ X-ray diffraction study of San Carlos olivine: influence of water on the 410 km seismic velocity jump in Earth's mantle. Am. Mineral. 96 (5–6), 697–702.
Conrad, P.G., Zha, C.S., Mao, H.K., Hemley, R.J., 1999. The high-pressure, single-crystal elasticity of pyrope, grossular, and andradite. Am. Mineral. 84, 374–383.
Dai, L.D., Li, H.P., Hu, H.Y., Shan, S.M., Jiang, J.J., Hui, K.S., 2012. The effect of chemical composition and oxygen fugacity on the electrical conductivity of dry and hydrous garnet at high temperatures and pressures. Contrib. Mineral. Petrol. 163, 689–700.
Dera, P., Zhuravlev, K., Prakapenka, V., Rivers, M.L., Finkelstein, G.J., Grubor-Urosevic, O., Tschauner, O., Clark, S.M., Downs, R.T., 2013. High pressure single-crystal micro X-ray diffraction analysis with GSE_ADA/RSV software. High Press. Res. 33, 466–484.
Du, W., Clark, S.M., Walker, D., 2015. Thermo-compression of pyrope-grossular garnet solid solutions: non-linear compositional dependence. Am. Mineral. 100, 215–222.
Duffy, T.S., Anderson, D.L., 1989. Seismic velocity in mantle minerals and mineralogy of the upper mantle. J. Geophys. Res. 94, 1895–1912.
Dymshits, A.M., Litasov, K.D., Shatskiy, A., Sharygin, I.S., Ohtani, E., Suzuki, A., Pokhilenko, N.P., Funakoshi, K., 2014. P-V-T equation of state of Na-majorite to 21 GPa and 1673 K. Phys. Earth Planet. Inter. 227, 68–75.
Dziewonski, A.M., Anderson, D.L., 1981. Preliminary reference Earth model. Phys. Earth Planet. Inter. 25, 297–356.
Fan, D.W., Zhou, W.G., Wei, S.Y., Liu, Y.G., Ma, M.N., Xie, H.S., 2010. A simple external resistance heating diamond anvil cell and its application for synchrotron radiation X-ray diffraction. Rev. Sci. Instrum. 81, 053903.
Fan, D.W., Ma, M.N., Wei, S.Y., Chen, Z.Q., Xie, H.S., 2013. High pressure elastic behavior of synthetic $Mg_3Y_2(SiO_4)_3$ garnet up to 9 GPa. Adv. Mater. Sci. Eng. 2013, 502702.
Fan, D.W., Xu, J.G., Ma, M.N., Wei, S.Y., Zhang, B., Liu, J., Xie, H.S., 2015. P-V-T equation of state of $Ca_3Cr_2Si_3O_{12}$ uvarovite garnet by using a diamond-anvil cell and in-situ synchrotron X-ray diffraction. Am. Mineral. 100, 588–597.
Fei, Y.W., Ricolleau, A., Frank, M., Mibe, K., Shen, G.Y., Prakapenka, V., 2007. Toward an internally consistent pressure scale. PNAS 104, 9182–9186.
Finkelstein, G.J., Dera, P.K., Duffy, T.S., 2015. Phase transitions in orthopyroxene (En90) to 49 GPa from single-crystal X-ray diffraction. Phys. Earth Planet. Inter. 244, 78–86.
Frost, D.J., 2008. The upper mantle and transition zone. Elements 4, 171–176.
Fumagalli, P., Klemme, S., 2015. Mineralogy of the earth: phase transitions and mineralogy of the upper mantle. In: Gerald Schubert (editor-in-chief) Treatise on Geophysics. . second ed., vol. 2 Elsevier, Oxford, pp. 7–31.
Gasparik, T., 2000. Evidence for immiscibility in majorite garnet from experiments at 13–15 GPa. Geochim. Cosmochim. Acta 64, 1641–1650.
Geiger, C.A., Langer, K., Bell, D.R., Rossman, G.R., Winkler, B., 1991. The hydroxide component in synthetic pyrope. Am. Mineral. 76, 49–59.
Gréaux, S., Kono, Y., Nishiyama, N., Kunimoto, T., Wada, K., Irifune, T., 2011. P-V-T equation of state of $Ca_3Al_2Si_3O_{12}$ grossular garnet. Phys. Chem. Miner. 38, 85–94.
Guyot, F., Wang, Y., Gillet, P., Ricard, Y., 1996. Quasiharmonic computations of thermodynamic parameters of olivines at high pressure and high temperature: a comparison with experiment data. Phys. Earth Planet. Inter. 98, 17–29.
Gwanmesia, G.D., Zhang, J.Z., Darling, K., Kung, J., Li, B.S., Wang, L.P., Neuville, D., Liebermann, R.C., 2006. Elasticity of polycrystalline pyrope ($Mg_3Al_2Si_3O_{12}$) to 9 GPa and 1000 °C. Phys. Earth Planet. Inter. 155, 179–190.
Hammersley, A.P., Svensson, S.O., Hanfland, M., Fitch, A.N., Hausermann, D., 1996. Two-dimensional detector software: from real detector to idealized image or two-theta scan. High Press. Res. 14, 235–248.
Hazen, R.M., Finger, L.W., 1978. Crystal structures and compressibilities of pyrope and grossular to 60 kbar. Am. Mineral. 63, 297–303.
Hickmott, D.D., 1989. Rare Earth Element Zoning in Pyrope-Rich Garnets from Mantle Xenoliths, Carnegie Institution, Washington Year Book 1988-1989, No. 2150, pp. 6–10.
Hickmott, D.D., Shimizu, N., Spear, F.S., Selverstone, J., 1987. Trace-element zoning in a metamorphic garnet. Geology 15, 573–576.
Hirschmann, M.M., 2006. Water, melting, and the deep earth H_2O cycle. Ann. Rev. Earth Planet. Sci. 34, 629–653.
Holl, C.M., Smyth, J.R., Jacobsen, S.D., Frost, D.J., 2008. Effects of hydration on the structure and compressibility of wadsleyite, β-(Mg_2SiO_4). Am. Mineral. 93, 598–607.
Huang, S., Chen, J.H., 2014. Equation of state of pyrope-almandine solid solution measured using a diamond anvil cell and in situ synchrotron X-ray diffraction. Phys. Earth Planet. Inter. 228, 88–91.
Huang, X., Xu, Y., Karato, S., 2005. Water content in the transition zone from electrical conductivity of wadsleyite and ringwoodite. Nature 434, 746–749.
Hunter, W.C., Smith, D., 1981. Garnet peridotite from colorado plateau ultramafic diatremes: hydrates, carbonates, and comparative geothermometry. Contrib. Mineral. Petrol. 76, 312–320.
Ingrin, J., Skogby, H., 2000. Hydrogen in nominally anhydrous upper-mantle minerals: concentration levels and implications. Eur. J. Mineral. 12, 543–570.
Irifune, T., Ringwood, A.E., 1987. Phase transformations in primitive MORB and pyrolite compositions to 25 GPa and some geophysical implications. In: Manghnani, M., Syono, Y. (Eds.), High Pressure Research in Mineral Physics, Geophysical Monograph Series, vol. 39. AGU, Washington, D. C., pp. 231–242.
Irifune, T., Ringwood, A.E., 1993. Phase transformations in subducted oceanic crust and buoyancy relationships at depths of 600–800 km in the mantle. Earth Planet. Sci. Lett. 117, 101–110.
Ita, J., Stixrude, L., 1992. Petrology, elasticity, and composition of the mantle transition zone. J. Geophys. Res. 97, 6849–6866.
Jackson, I., Rigden, S.M., 1996. Analysis of P-V-T data: constraints on the thermoelastic properties of high-pressure minerals. Phys. Earth Planet. Inter. 96, 85–112.
Jacobsen, S.D., 2006. Effect of water on the equation of state of nominally anhydrous minerals. In: Keppler, H.J., Smyth, J.R., (Eds.). Water in Nominally Anhydrous Minerals, 62, p. 321–342. Rev. Mineral. Geochem., Mineralogical Society of America, Chantilly, Virginia.

Jiang, F.M., Speziale, S., Duffy, T.S., 2004. Single-crystal elasticity of grossular- and almandine-rich garnets to 11 GPa by Brillouin scattering. J. Geophys. Res. 109, B10210.

Jung, H., Karato, S., 2001. Water induced fabric transitions in olivine. Science 293, 1460–1463.

Karato, S., 1990. The role of hydrogen in the electrical conductivity of the upper mantle. Nature 347, 272–273.

Karato, S., 2006. Influence of hydrogen-related defects on the electrical conductivity and plastic deformation of mantle minerals: a critical review. In: Jacobsen, S.D., van der Lee, S. (Eds.), Earth's Deep Water Cycle, 168. American Geophysical Union, Geophysical Monograph Series, Washington, D.C., pp. 113–129.

Katsura, T., Yoneda, A., Yamazaki, D., Yoshino, T., Ito, E., 2010. Adiabatic temperature profile in the mantle. Phys. Earth Planet. Inter. 183, 212–218.

Kavner, A., 2003. Elasticity and strength of hydrous ringwoodite at high pressure. Earth Planet. Sci. Lett. 214, 645–654.

Keshav, S., Sen, G., Presnall, D.C., 2007. Garnet-bearing xenoliths from salt lake crater, Oahu, Hawaii: high-pressure fractional crystallization in the oceanic mantle. J. Petrol. 48, 1681–1724.

Kohlstedt, D.L., Keppler, H., Rubie, D.C., 1996. Solubility of water in the α-phase, β-phase and γ-phase of $(Mg, Fe)_2SiO_4$. Contrib. Min. Petrol. 123, 345–357.

Kono, Y., Gréaux, S., Higo, Y., Ohfuji, H., Irifune, T., 2010. Pressure and temperature dependences of elastic properties of grossular garnet up to 17 GPa and 1650 K. J. Earth Sci. 21, 782–791.

Kubo, T., Ohtani, E., Kato, T., Shinmei, T., Fujino, K., 1998. Effect of water on the α–β transformation kinetics in San Carlos olivine. Science 281, 85–87.

Kubo, T., Ohtani, E., Kondo, T., Kato, T., Toma, M., Hosoya, T., Sano, A., Kikegawa, T., Nagase, T., 2002. Metastable garnet in oceanic crust at the top of the lower mantle. Nature 420, 803–806.

Lager, G.A., Downs, R.T., Origlieri, M., Garoutte, R., 2002. High-pressure single-crystal X-ray diffraction study of katoite hydrogarnet: evidence for a phase transition from *Ia3d* to *I43d* symmetry at 5 GPa. Am. Mineral. 87, 642–647.

Lager, G.A., Marshall, W.G., Liu, Z., Downs, R.T., 2005. Re-examination of the hydrogarnet structure at high pressure using neutron powder diffraction and infrared spectroscopy. Am. Mineral. 90, 639–644.

Larson, A.C., Von Dreele, R.B., 2000. GSAS general structure analysis system operation manual. Los Alamos Natl. Lab. 86–748, 1–179.

Le Bail, A., Duroy, H., Fourquet, J.L., 1988. Ab initio structure determination of $LiSbWO_6$ by X-ray powder diffraction. Mater. Res. Bull. 23, 447–452.

Leger, J.M., Redon, A.M., Chateau, C., 1990. Compressions of Synthetic Pyrope, Spessartine and Uvarovite Garnets up to 25 GPa. Phys. Chem. Miner. 17, 161–167.

Leitner, B.J., Weidner, D.J., Liebermann, R.C., 1980. Elasticity of single crystal pyrope and implications for garnet solid solution series. Phys. Earth Planet. Inter. 22, 111–121.

Levien, L., Prewitt, C.T., Weidner, D.J., 1979. Compression of pyrope. Am. Mineral. 64, 805–808.

Li, L., Weidner, D.J., Brodholt, J., Alfe, D., Price, G.D., 2011. Ab initio molecular dynamic simulation on the elasticity of $Mg_3Al_2Si_3O_{12}$ pyrope. J. Earth Sci. 22, 169–175.

Liu, W., Li, B.S., 2006. Thermal equation of state $(Mg_{0.9}Fe_{0.1})_2SiO_4$ olivine. Phys. Earth Planet. Inter. 157, 188–195.

Lu, R., Keppler, H., 1997. Water solubility in pyrope to 100 kbar. Contrib. Min. Petrol. 129, 35–42.

Lu, C., Mao, Z., Lin, J.F., Zhuravlev, K.K., Tkachev, S.N., Prakapenka, V.B., 2013. Elasticity of single-crystal iron-bearing pyrope up to 20 GPa and 750 K. Earth Planet. Sci. Lett. 361, 134–142.

Mao, H.K., Bell, P.M., Shaner, J.W., Steinberg, D.J., 1978. Specific volume measurements of Cu, Mo, Pd, and Ag and calibration of the ruby R1 fluorescence pressure gauge from 0.06 to 1 Mbar. J. Appl. Phys. 49, 3276–3283.

Mei, S., Kohlstedt, D.L., 2000. Influence of water on plastic deformation of olivine aggregates 1. Diffusion creep regime. J. Geophys. Res. 105, 21457–21469.

Mookherjee, M., Karato, S., 2010. Solubility of water in pyrope-rich garnet at high pressures and temperature. Geophys. Res. Lett. 37, L03310.

Nishihara, Y., Takahashi, E., Matsukage, K.N., Kikegawa, T., 2003. Thermal equation of state of omphacite. Am. Mineral. 88, 80–86.

Nishihara, Y., Takahashi, E., Matsukage, K.N., Iguchi, T., Nakayama, K., Funakoshi, K., 2004. Thermal equation of state $(Mg_{0.91}Fe_{0.09})_2SiO_4$ ringwoodite. Phys. Earth Planet. Inter. 143–144, 33–46.

O'Neill, B., Bass, J.D., Rossman, G.R., 1993. Elastic properties of hydrogrossular garnet and implications for water in the upper mantle. J. Geophys. Res. 98, 20031–20037.

Ohtani, E., 2005. Water in the Mantle. Elements 1, 25–30.

Olijnyk, H., Paris, E., Geiger, C.A., Lager, G.A., 1991. Compressional study of katoite $[Ca_3Al_2(O_4H_4)_3]$ and grossular garnet. J. Geophys. Res. 96, 14313–14318.

Passaglia, E., Rinaldi, R., 1984. Katoite, a new member of the $Ca_3Al_2(SiO_4)_3$-$Ca_3Al_2(OH)_{12}$ series and a new no-menclature for the hydrogrossular group of minerals. Bull. Minéral. 107, 605–618.

Pavese, A., Diella, V., Pischedda, V., Merli, M., Bocchio, R., Mezouar, M., 2001. Pressure-volume-temperature equation of state of andradite and grossular, by high-pressure and -temperature powder diffraction. Phys. Chem. Miner. 28, 242–248.

Piermarini, G.J., Block, S., Barnett, J.D., 1973. Hydrostatic limits in liquids and solids to 100 kbar. J. Appl. Phys. 44, 5377–5382.

Pigott, J.S., Wright, K., Gale, J.D., Panero, W.R., 2015. Calculation of the energetic of water incorporation in majorite garnet. Am. Mineral. 100, 1065–1075.

Ringwood, A.E., 1975. Composition and Petrology of the Earth's Mantle. McGraw-Hill, New York.

Ringwood, A.E., 1991. Phase transformations and their bearing on the constitution and dynamics of the mantle. Geochim. Cosmochim. Acta 55, 2083–2110.

Rossman, G.R., 1996. Studies of OH in nominally anhydrous minerals. Phys. Chem. Miner. 23, 299–304.

Rossman, G.R., Aines, R.D., 1991. The hydrous components in garnets: grossular–hydrogrossular. Am. Mineral. 76, 1153–1164.

Rossman, G.R., Smyth, J.R., 1990. Hydroxyl contents of accessory minerals in mantle eclogites and related rocks. Am. Mineral. 75, 775–780.

Saltzer, R.L., Chatter Jee, N., Grove, T.L., 2001. The spatial distribution of garnets and pyroxenes in mantle peridotites: pressure-temperature history of peridotites from the Kaapvaal craton. J. Petrol. 42, 2215–2229.

Sato, Y., Akaogi, M., Akimoto, S., 1978. Hydrostatic compression of the synthetic garnets pyrope and almandine. J. Geophys. Res. 83, 335–338.

Shim, S., Duffy, T.S., Shen, G., 2000. The stability and P-V-T equation of state of $CaSiO_3$ perovskite in the Earth's lower mantle. J. Geophys. Res. 105, 25955–25968.

Shinmei, T., Tomioka, N., Fujino, K., Kuroda, K., Irifune, T., 1999. In situ X-ray diffraction study of enstatite up to 12 GPa and 1473 K and equations of state. Am. Mineral. 84, 1588–1594.

Sinogeikin, S.V., Bass, J.D., 2000. Single-crystal elasticity of pyrope and MgO to 20 GPa by Brillouin scattering in the diamond cell. Phys. Earth Planet. Inter. 120, 43–62.

Sinogeikin, S.V., Bass, J.D., 2002a. Elasticity of majorite and a majorite-pyrope solid solution to high pressure: implications for the transition zone. Geophys. Res. Lett. 29. http://dx.doi.org/10.1029/2001GL013937.

Sinogeikin, S.V., Bass, J.D., 2002b. Elasticity of pyrope and majorite-pyrope solid solutions to high temperatures. Earth Planet. Sci. Lett. 203, 549–555.

Skogby, H., 2006. Water in natural mantle minerals I: Pyroxenes. Rev. Mineral. Geochem. 62, 155–167.

Skogby, H., Bell, D.R., Rossman, G.R., 1990. Hydroxide in pyroxene: variations in the natural environment. Am. Mineral. 75, 764–774.

Smyth, J.R., Jacobsen, S.D., 2006. Nominally anhydrous minerals and Earth's deep water cycle. In Jacobsen, S.D., van der lee, S., (Eds.). Earth's Deep Water Cycle, 168, p. 1–11. Monograph Series, American Geophysical Union, Washington, D.C.

Smyth, J.R., Bell, D.R., Rossman, G.R., 1991. Incorporation of hydroxyl in upper-mantle clinopyroxenes. Nature 351, 732–735.

Smyth, J.R., Jacobsen, S.D., Hazen, R.M., 2000. Comparative crystal chemistry of orthosilicate minerals. Rev. Mineral. Geochem. 41, 187–209.

Smyth, J.R., Holl, C.M., Frost, D.J., Jacobsen, S.D., Langenhorst, F., McCammon, C.A., 2003. Structural systematics of hydrous ringwoodite and water in Earth's interior. Am. Mineral. 88, 1402–1407.

Smyth, J.R., Frost, D.J., Nestola, F., 2005. Hydration of olivine and the Earth's deep water cycle. Geochim. Cosmochim. Acta 69, A746.

Smyth, J.R., Mierdel, K., Keppler, H., Langenhorst, F., Dubrovinsky, L., Nestola, F., 2007. Crystal chemistry of hydration in aluminous orthopyroxene. Am. Mineral. 92, 973–976.

Suzuki, I., Anderson, O.L., 1983. Elasticity and thermal expansion of a natural garnet up to 1000 K. J. Phys. Earth 31, 125–138.

Tenner, T.J., Hirschmann, M.M., Withers, A.C., Hervig, R.L., 2009. Hydrogen partitioning between nominally anhydrous upper mantle minerals and melt between 3 and 5 GPa and applications to hydrous peridotite partial melting. Chem. Geol. 262, 42–56.

Tenner, T.J., Hirschmann, M.M., Withers, A.C., Ardia, P., 2012. H_2O storage capacity of olivine and low-Ca pyroxene from 10 to 13 GPa: consequences for dehydration melting above the transition zone. Contrib. Min. Petrol. 163, 297–316.

Toby, B.H., 2001. EXPGUI, a graphical user interface for GSAS. J. Appl. Crystallogr. 34, 210–213.

Wang, Z.C., Ji, S.C., 2001. Elasticity of six polycrystalline silicate garnets at pressure up to 3.0 GPa. Am. Mineral. 86, 1209–1218.

Wang, Y., Weinder, D.J., Guyot, F., 1996. Thermal equation of state of $CaSiO_3$ perovskite. J. Geophys. Res. 101, 661–672.

Wang, Y.B., Weidner, D.J., Zhang, J.Z., Gwanrnesia, G.D., Liebermann, R.C., 1998. Thermal equation of state of garnets along the pyrope-majorite join. Phys. Earth Planet. Inter. 105, 59–71.

Weidner, D.J., Wang, Y., 2000. Phase transformations: implications for mantle structure. In: Karato, S.I. et al. (Eds.), Earth's Deep Interior: Mineral Physics and Tomography From the Atomic to the Global Scale, Geophysical Monograph Series, vol. 117. AGU, Washington, D. C., pp. 215–235.

Williams, Q., Hemley, R.J., 2001. Hydrogen in the deep Earth. Ann. Rev. Earth Planet. Sci. 29, 365–418.

Withers, A.C., Wood, B.J., Carroll, M.R., 1998. The OH content of pyrope at high pressure. Chem. Geol. 147, 161–171.

Woodland, A.B., 1998. The orthorhombic to high-P monoclinic phase transition in Mg-Fe pyroxenes: can it produce a seismic discontinuity? Geophys. Res. Lett. 25, 1241–1244.

Xie, H.S., Zhang, Y., Xu, H.G., Hou, W., Guo, J., Zhao, H., 1993. A new method of measurement for elastic wave velocities in minerals and rocks at high temperature and high pressure and its significance. Sci. China Chem. 36, 1276–1280.

Xie, H.S., Zhou, W.G., Liu, Y.G., Guo, J., Hou, W., Zhao, Z.D., 2002. Comparative experimental study on several methods for measuring elastic wave velocities in rocks at high pressure. Sci. China Earth Sci. 45, 990–998.

Yagi, T., Akaogi, M., Shimomura, O., Tamai, H., Akimoto, S., 1987. High pressure and high temperature equations of state of majorite. In: Syono, Y., Manghnani, M.H. (Eds.), High Pressure Research in Mineral Physics. Terrapub, Tokyo, pp. 141–147.

Ye, Y., Smyth, J.R., Hushur, A., Manghnani, M.H., Lonappan, D., Dera, P., Frost, D.J., 2010. Crystal structure of hydrous wadsleyite with 2.8% H_2O and compressibility to 60 GPa. Am. Mineral. 95, 1765–1772.

Ye, Y., Brown, D.A., Smyth, J.R., Panero, W.R., Jacobsen, S.D., Chang, Y.Y., Townsend, J.P., Thomas, S.M., Hauri, E.H., Dera, P., Frost, D.J., 2012. Compressibility and thermal expansion of hydrous ringwoodite with 2.5(3) wt% H_2O. Am. Mineral. 97, 573–582.

Yu, Y.G., Wentzcovitch, R.M., 2009. Low-pressure clino- to high-pressure clinoenstatite phase transition: a phonon-related mechanism. Am. Mineral. 94, 461–466.

Zhang, L., Ahsbahs, H., Kutoglu, A., 1998. Hydrostatic compression and crystal structure of pyrope to 33 GPa. Phys. Chem. Miner. 25, 301–307.

Zhang, D.Z., Jackson, J.M., Chen, B., Sturhahn, W., Zhao, J.Y., Yan, J.Y., Caracas, R., 2013. Elasticity and lattice dynamics of enstatite at high pressure. J. Geophys. Res. 118, 4071–4082.

Zhao, Y.S., Schiferl, D., Shankland, T.J., 1995. A high P-T single-crystal X-ray diffraction study of thermoelasticity of $MgSiO_3$ orthoenstatite. Phys. Chem. Miner. 22, 393–398.

Zhao, Y.S., Von Dreele, R.B., Zhang, J.Z., Weidner, D.J., 1998. Thermoelastic equation of state of monoclinic pyroxene $CaMgSi_2O_6$ diopside. Rev. High Press. Sci. Technol. 7, 25–27.

Zou, Y.T., Gréaux, S., Irifune, T., Whitaker, M.L., Shinmei, T., Higo, Y., 2012. Thermal equation of state of $Mg_3Al_2Si_3O_{12}$ pyrope garnet up to 19 GPa and 1700 K. Phys. Chem. Miner. 39, 589–598.